



Wire Arc Additive Manufacturing of AISI 420 Martensitic Stainless Steel: On As-Printed Microstructure and Mechanical Properties

Jonas Lunde, Mostafa Kazemipour, Salar Salahi, and Ali Nasiri

Submitted: 5 April 2021 / Revised: 3 July 2021 / Accepted: 14 July 2021 / Published online: 17 August 2021

In this study, the microstructure and mechanical properties of an AISI 420 martensitic stainless steel multilayer single-bead part produced by wire arc additive manufacturing were investigated. To characterize the microstructure and mechanical properties of different zones of the printed wall, samples were prepared from the bottom, middle and top regions along the part's building direction. Microstructural analyses revealed the formation of a martensitic matrix along with delta ferrite and retained austenite as secondary phases in the as-printed microstructure. The presence of these secondary phases was correlated with the complex thermal history in the deposited layers associated with cyclic re-heating and cooling as subsequent layers were deposited. Higher hardness values were measured for the top region of the fabricated parts since these layers were not exposed to the same in situ re-heating cycles as the bottom and middle layers. Uniaxial tensile tests along the building and deposition directions revealed similar low elongation and high tensile strength for the bottom and middle regions. Differently, the samples from the top region fractured at a lower strength and elongation due to their harder nature of untempered martensitic matrix combined with the deteriorating effect of a significantly higher amount of delta ferrite in the top region.

Keywords 420 stainless steel, mechanical properties, microstructure, wire arc additive manufacturing

1. Introduction

The advancements in the field of metal additive manufacturing (AM) in recent years have given various industries the opportunity of rapid fabrication of intricate components in an incremental layer-by-layer fashion (Ref 1). As compared to the subtractive fabrication methods, *e.g.*, casting, forming or machining, AM is capable of producing intricate components with fewer design complications and more economically efficient due to the lower material waste, leading to a shorter lead time (Ref 2). Although there are multiple ways of producing parts through metal AM, the two commonly used techniques are powder bed fusion (PBF) and direct energy deposition (DED). Although the DED techniques cannot compete with the PBF capabilities in fabricating complex components, they are able to produce significantly larger parts with a less complex design much faster at drastically lower fabrication cost (Ref 3). A common method of DED often termed as wire arc additive manufacturing (WAAM) involves the feeding of the feedstock metal wire at a controlled rate

through a welding torch-produced arc or plasma, mounted on a multi-axis robotic arm or a CNC-gantry system. As a droplet-based 3D printing method, WAAM is well suited for producing components with simple to medium complexity (Ref 4). A wide range of materials can be fabricated using WAAM technology, such as stainless steels, HSLA steels and Ti alloys (Ref 5-7). As compared to the laser-based or electron beam-based AM processes, using electric arc as the heat source in the WAAM contributes to a more moderate rate of heating and cooling during fabrication and can produce parts with fewer defects (Ref 8, 9).

Compared to most conventional manufacturing methods, a component produced by the WAAM experiences a more complicated thermal history during fabrication involving multiple cycles of heating and cooling, leading to the formation of a more inhomogeneous solidification structure (Ref 10, 11). Such frequent heating and cooling cycles are attributed to the deposition of subsequent layers during the manufacturing process (Ref 12). Therefore, the obtained microstructure and mechanical properties of a WAAM part are commonly different from its wrought or entirely cast counterpart (Ref 13). The inhomogeneous microstructure and undesirable microconstituents in AM-fabricated products commonly provoke anisotropic mechanical properties (Ref 14), which emphasizes on the need to control the microstructure either during the printing process or through applying appropriate post-printing heat treat cycles (Ref 15, 16). In a recent study by Hejripour et al. (Ref 17), the yield strength and elongation of samples along the horizontal and building directions for a WAAM-fabricated duplex stainless steel were compared, and a higher yield strength but lower elongation was reported for the horizontal samples. Similar results were obtained by Griffith et al. (Ref 18) when studying the microstructure and mechanical properties of 316 and 304L stainless steel components produced by laser

Jonas Lunde, Mostafa Kazemipour, and Salar Salahi, Faculty of Engineering and Applied Science, Memorial University of Newfoundland, St. John's, NL A1B 3X5, Canada; and **Ali Nasiri**, Faculty of Engineering and Applied Science, Memorial University of Newfoundland, St. John's, NL A1B 3X5, Canada; and Department of Mechanical Engineering, Dalhousie University, 1360 Barrington St, Halifax, NS B3H 4R2, Canada. Contact e-mail: jhlunde@mun.ca.

engineered net shaping, reporting a higher yield strength at the cost of ductility for the horizontal specimens.

The AISI 420 martensitic stainless steel (MSS) is considered a general-purpose alloy and is mainly used in applications where an excellent combination of resistance to corrosion and good mechanical properties are required (Ref 19–21). MSSs usually contain between 11.5 and 18 wt.% chromium and up to 0.6 wt.% carbon and form a martensitic microstructure when quenched from austenitizing temperatures (Ref 22–24). The corrosion resistance of stainless steels (SS) in general is associated with the formation of a 1-3-nm-thick passive oxide film on the surface of the alloy (Ref 25). Although many other grades of SS can provide better corrosion performance in harsh environments, AISI 420 is the commonly used alloy due to its lower cost (Ref 26). However, there is little published research on the use of the WAAM technology to produce parts using AISI 420 feedstock wire. The high cooling rate associated with the welding of MSSs can lead to the supercooling of delta ferrite phase during its transformation to austenite, making it possible for undesirable delta ferrite to coexist with retained austenite and martensite at room temperature (Ref 27–29). Baghjari et al. (Ref 30) studied the laser welding of AISI 420 SS and reported the formation of delta ferrite along with carbide precipitates in a martensitic matrix. The formation and stabilization of delta ferrite at room temperature has been also reported in the structure of other grades of AM-fabricated stainless steels, such as 304 SS, at various heat input levels (Ref 31). Ge et al. (Ref 10) in their study of a 2Cr13 (containing approximately half the amount of carbon as the alloy in the present study) thin-wall part produced by cold metal transfer (CMT) WAAM reported that the martensite content increases from the bottom of the fabricated wall to the top. The formation of austenite in the microstructure of a WAAM-2Cr13 was also reported in a different study by Ge et al. (Ref 32), when they used a shorter interlayer dwell time during fabrication.

Implementing the WAAM technology for fabrication of parts from the MSS family and in particular AISI 420 SS is relatively new, and the open literature on this subject is very limited. More detailed studies of the topic are required to clearly elucidate the process–microstructure–performance correlations in the fabricated parts, especially when various modes of metal transfer are adopted during the fabrication process. This study investigates the microstructural variations along the building direction and the resulting anisotropic mechanical response of an as-printed multilayer single-bead thickness wall of AISI 420 SS produced by the state-of-the-art surface tension transfer (STT) WAAM technology. The mechanical properties of the deposited wall were investigated by microhardness and uniaxial tensile tests, along with fractography of the fractured surfaces of the tensile specimens. The purpose of the performed study was to determine how the complex WAAM thermal history affected the microconstituents formation in the microstructure and their effect on the mechanical properties of the fabricated part.

2. Experimental Procedure

A multilayer wall with the length, height and thickness of 150, 75 and 10 mm, respectively, was fabricated through the WAAM technology using ER420 SS feedstock wire on a wrought AISI 420 base plate. The illustration of the fabricated

wall is shown in Fig. 1. For fabrication of the wall, a six-axis robotic arm was used for consistent and uniform deposition of the material. This robotic arm utilized an all-y scanning strategy with alternating directions. The chemical composition of the used wire and base plate and the process parameters used for deposition are displayed in Tables 1 and 2, respectively. To ensure the consistent interlayer temperature of 200 °C prior to the deposition of each layer, the temperature of each newly deposited layer was monitored using a laser thermometer. For characterization of the microstructure and mechanical properties, the wall was divided into three different regions, including the bottom, middle and top areas with the base plate as a reference point (see Fig. 1). To prepare flat horizontal and vertical tensile samples, the wall was cut from the base plate and ground until a smooth and level surface was achieved, which decreased its thickness to 5 mm. The position of the horizontal and vertical uniaxial tensile test samples with the gauge dimensions of 30 × 10 × 2 mm prepared from the wall, along the deposition and building directions, are illustrated in Fig. 1. The uniaxial tensile testing of the samples was conducted at the strain rate of 1 mm/min. The displacement data from each sample during tensile testing were gathered using an extensometer attached to the specimen's gauge and the yield strength was calculated using the 0.2% offset method. Vickers microhardness measurements were also taken covering three regions. The hardness profile included multiple layers within each region, which were large enough to have a center region distinguishable from heat-affected zones and melt pool boundaries. For characterizing the microstructure, samples from each region were cut, ground, polished, following standard sample preparation procedures for MSS, and etched with Vilella's etchant before being examined by an FEI MLA 650F scanning electron microscope (SEM) to determine the microstructure. The SEM was also equipped with a Bruker energy-dispersive x-ray (EDX) analytical system to map concentrations of the chemical elements and an HKL electron backscatter diffraction (EBSD) system. The inverse pole figures (IPFs), pole figures (PFs), grain boundary maps and phase maps were obtained using the EBSD analysis. Only data

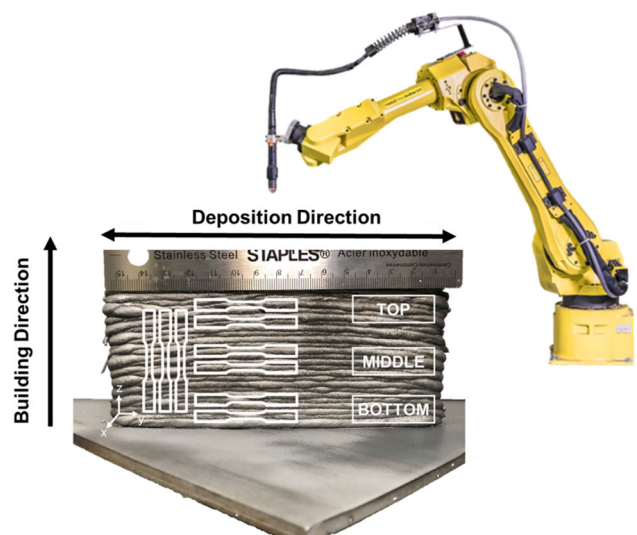


Fig. 1 Illustration of the WAAM-deposited wall and the robot used for the deposition along with some of the locations of the extracted tensile samples and the three investigated regions

Table 1 Nominal chemical composition of the used feedstock wire and the base metal (all data in wt.%)

Sample	Cr	C	Si	Mn	Ni	Mo	P	S	Cu	V	Fe
AISI-420 base metal	12-14	0.15-0.46	0-1	0.4-1	...	0-0.1	0-0.04	0-0.03	...	0.3	Bal.
ER-420 wire	12-14	0.3-0.4	0-1	0-1	0-0.5	0-0.5	0-0.04	0-0.03	0-0.5	...	Bal.

Table 2 Process parameters used during deposition of the multilayer wall

Wire feed speed	Travel speed	Current	Gas flow rate	Arc voltage	Wire size
4.06 m/min	0.22 m/min	135 A	45 L/min	29 V	0.11 cm

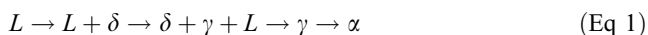
points with confidence index higher than 0.01 were considered valid in the performed EBSD analysis herein. To post-process the collected EBSD raw data, Channel 5 software was used. X-ray diffraction (XRD) analysis was also conducted using an Ultima-IV XRD diffractometer to determine the phases present in the microstructure. Cu-K_α radiation ($\lambda=1.54\text{\AA}$) within a 2θ -range of 20-100° using 1° min⁻¹ scanning rate were the measuring parameters. The MDI JADE 2010 software was used to determine the volume fractions of the phases in each region employing the whole pattern fitting (WPF) technique.

3. Results and Discussion

3.1 Microstructure

3.1.1 SEM Analysis. The SEM images taken from the bottom, middle and the top regions of the fabricated wall are shown in Fig. 2. Figure 2(a) and (d) shows the micrograph depicting the microstructure of the bottom and middle regions, respectively, revealing a coarse martensitic matrix denoted as α' phase. A noticeable change can be detected in the microstructure of the top region (Fig. 2g) as compared to the bottom and middle regions. The top region's microstructure contains a high-volume fraction of vermicular-shaped delta ferrite denoted as δ as an additional phase formed along the primary austenite grain boundaries embedded in a martensitic matrix. The SEM images shown in Fig. 2(a) and (d) also revealed the formation of a less continuous network of delta ferrite phase (δ), as compared to the top region, along with the martensite. The EDX concentration maps taken from the microstructure of different regions of the fabricated part also shown in Fig. 2 confirmed the positions of delta ferrite phase along the interdendritic regions, where higher concentrations of Cr element (a ferrite stabilizing element) and lower concentration of iron as compared to the surrounding matrix were detected.

Figure 3 depicts the Fe-Cr-C pseudo-binary phase diagram for a SS containing 13 wt.% chromium (modified from (Ref 33)). The solidification process of an AISI 420 SS containing approximately 0.35 wt.% carbon during equilibrium conditions is indicated on the phase diagram and described in Eq 1, where L, δ , γ and α correspond to the liquid, delta ferrite, austenite and ferrite phases, respectively.



As already mentioned, the WAAM process can resemble a multi-pass arc welding process. Analogously, a non-equilibrium solidification is expected during WAAM ascribed to the high cooling rate associated with the process. Therefore, the equilibrium solidification path shown in Fig. 3 and equation (1) will not be followed strictly during deposition and solidification of each individual layer of the fabricated wall studied herein. Consequently, instead of obtaining a fully ferritic microstructure in as-printed condition, the high cooling rate of the WAAM leads to the formation of primarily a martensitic matrix (Ref 34). If in the chemical composition of the martensitic SS, the content of ferrite stabilizing elements dominates over the austenite stabilizing elements (the case of ER420), it is possible for high-temperature delta ferrite phase to be retained in the martensitic matrix at room temperature. It has been also reported that very high cooling rates during laser welding can prevent the delta ferrite to austenite transformation (Ref 30). The chemical composition of the feedstock wire used in this study contains a relatively low amount of austenite stabilizers as compared to ferrite stabilizing elements, which allowed for the aforementioned retaining of delta ferrite in the microstructure at room temperature. The presence of delta ferrite in the microstructure of a duplex SS produced by WAAM has been also reported, and the concentration of chromium found in the delta ferrite phase was ~ 5% higher than that of the wire used for deposition (Ref 17). The observed higher content of chromium in the delta ferrite phase formed along the interdendritic regions (~17 wt.% Cr) in this study (seen in Fig. 2b,e,h) corresponds well with these findings. The observed vermicular-shaped delta ferrite phase differentiates the detected as-printed microstructure of the fabricated alloy herein compared to that reported in previous studies on WAAM of 13Cr martensitic stainless steels (Ref 10, 32, 35, 36).

The stabilization of retained austenite at room temperature in the microstructure can be justified if the martensite finish (M_f) temperature of the alloy is below the room temperature (Ref 37). The M_f temperature of AISI 420 can be considered to be 150-200°C lower than the martensite start (M_s) temperature (Ref 22). Several equations for calculation of M_s have been reported in previous studies and are listed in Table 3. Using the average values of the provided ranges in Table 1 for the chemical composition of the ER420 feedstock wire, the M_s temperature of the alloy was calculated, employing all M_s equations in Table 3. As given in Table 3, the M_f temperature ranges include temperatures below room temperature, confirm-

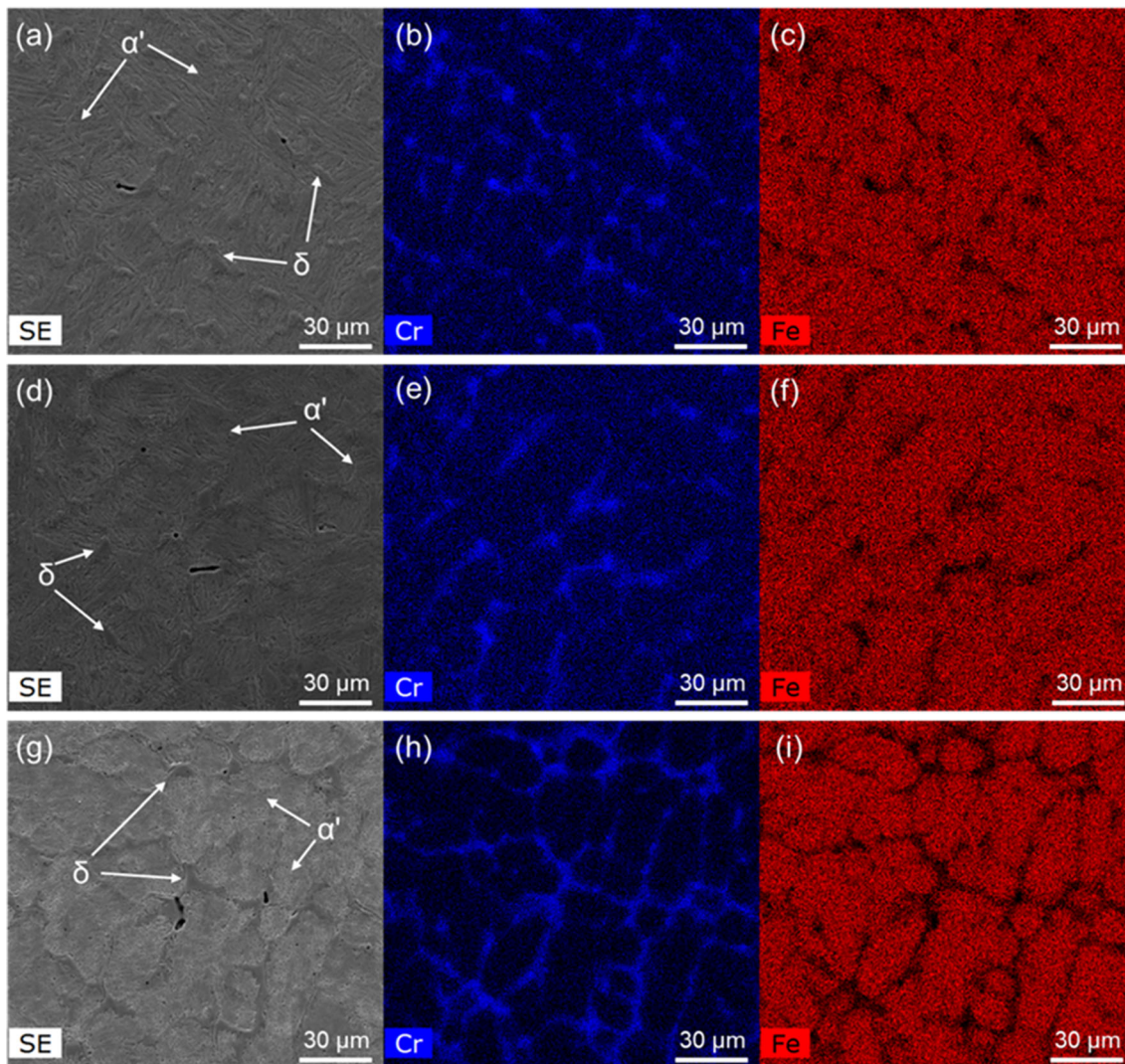


Fig. 2 SEM images and EDX elemental maps indicating Cr and Fe concentrations taken from the (a-c) bottom, (d-f) middle and (g-i) top regions of the WAAM-fabricated ER420 wall

ing that the retained austenite can stay stable in the final as-printed microstructure of this alloy at room temperature. The presence of retained austenite in stainless steels parts produced by AM has been also reported in previous studies (Ref 38, 39). Austenite contents of as high as 57% have been documented in parts of AISI 420 produced by selective laser melting due to exposure to thermal cycling during deposition (Ref 38). It is also reported that WAAM processing parameters can affect the presence and content of retained austenite in the microstructure of 17-4 PH stainless steel (Ref 39). As a result of ambient temperature around the austenite reversion temperature range, the dwelling time between the deposition of each layer can significantly affect the content of retained austenite in the produced part (Ref 32). As the layers of the manufactured wall in the present study were deposited onto the previously solidified layer at a temperature of 200 °C, the fabrication condition herein is analogous to a short interlayer dwelling time. As a new layer is deposited, the heat associated with the deposition affects the underlying layers, with the closer layers experiencing higher temperatures than the deeper underlying

layers from the new deposit. Potentially, the closer layers can reach the austenitizing temperatures, and consequently, their martensite matrix can partially/locally retransform to austenite. This austenite can be partially retained in the martensitic matrix as it cools down (Ref 40). The 420 MSS alloy contains a relatively high amount of carbon content, contributing to a high level of tetragonality in the formed martensite phase from this alloy. Subsequently, the layers being deposited provide enough heat energy to raise the temperature of the previously solidified layers above their M_s temperature, causing carbon diffusion from the saturated martensite to the austenite phase with higher carbon solubility (Ref 41). The higher carbon content in the alloy is expected to decrease both M_s and M_f temperatures based on the martensite transition temperatures shown in Table 3, which causes further austenite stabilization at room temperature. These higher temperatures associated with the deposition of new layers also caused the less continuous network of delta ferrite phase in the bottom and middle regions, as some of the delta ferrite phase in these regions were

retransformed to austenite and subsequently transformed into martensite upon cooling.

3.1.2 XRD Analysis. The XRD patterns obtained from three regions, *i.e.*, the bottom, middle and the top of the WAAM-ER420 wall are shown in Fig. 4. Consistent with the results obtained from the OM and SEM analysis, the XRD spectra revealed austenite peaks alongside the martensite peaks. Four diffraction peaks for each of the two phases were detected, (110), (200), (211) and (220) for martensite and (111), (200), (220) and (311) for austenite. Even though diffraction peaks for alpha ferrite, delta ferrite and martensite are not possible to be distinguished due to their similar lattice axis ratio (Ref 42), the SEM analysis results (Fig. 2) determined that the peaks belonged to both martensite and delta ferrite. The similar XRD patterns found for the bottom and middle regions indicate that the in situ re-heating effect associated with newer deposited layers have affected these regions equally. Using the WPF technique, the volume fractions of austenite in the bottom, middle and top regions were found to be 17.4, 18.2 and 20.6%, respectively, further confirming the retransformation of some austenite to martensite in more frequently tempered bottom

layers.

3.1.3 EBSD Analysis. Figure 5 shows the IPF maps superimposed on grain boundaries maps (Fig. 5a-c) and phase maps (Fig. 5d-f) of the as-printed part taken from the bottom, middle and top regions of the fabricated part, all prepared from the center of each deposited layer and along the building direction (BD). Regardless of the position of the sample along the BD, a lath martensitic structure is formed in all layers (Fig. 5a-c). The formed martensite laths are mostly aligned with the building direction with relatively coarse structure while randomly oriented blocky martensite are observed as well. The average lath size of the martensite decreased slightly from the bottom to the top region, with values of 0.76, 0.71 and 0.65 μm for the bottom, middle and top, respectively. This indicates that fewer in situ re-heating cycles for the more top layers have led to less grain growth. Phase maps of different regions are extracted from the EBSD data and illustrated in Fig 5(d), (e) and (f). The body-centered cubic (BCC) structure stands for both the delta ferrite phase and the tempered martensitic laths, formed in the structure. Although making a distinction between the ferrite and martensitic phase is not practical through EBSD analysis, it is observed that the fraction of martensite phase remains relatively constant in all regions. A significant fraction

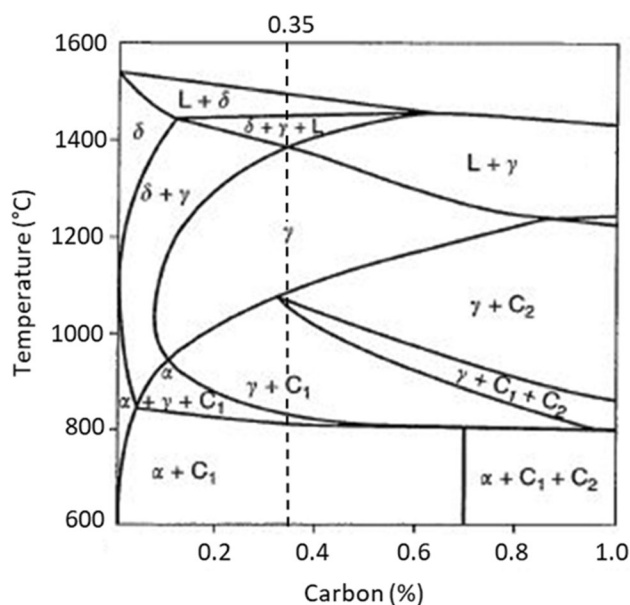


Fig. 3 Pseudo-binary phase diagram of an MSS containing 13 wt.% chromium with the carbon content in the present study taken as the average of its range (0.35 wt.%) indicated by the dashed line (modified from (Ref 33))

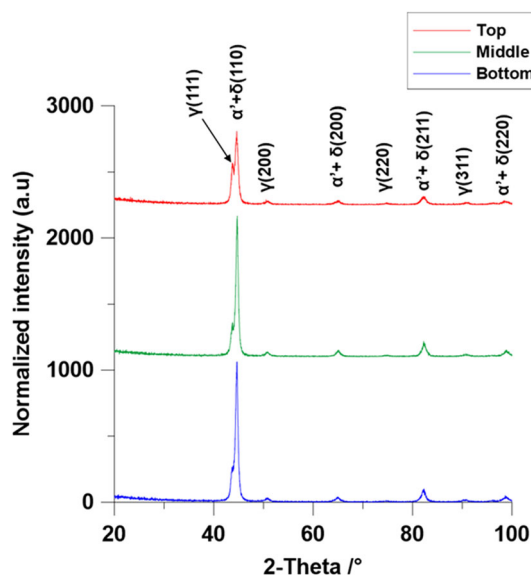


Fig. 4 XRD patterns of the bottom, middle and the top regions of the WAAM-ER420 wall with annotated peaks for martensite and delta ferrite ($\alpha'+\delta$) and austenite (γ)

Table 3 Martensite start temperature (M_s) equations gathered from the literature

Reference	M_s equation	M_s , °C	M_f , °C
Irvine et al. (Ref 61)	$551 - (474C + 33Mn + 11Si + 17Cr + 17Ni + 21Mo + 11W)$	183.6	[-16.4, 33.6]
Steven and Haynes (Ref 62)	$561 - (474C + 33Mn + 17Cr + 17Ni + 21Mo)$	148.1	[-51.9, -1.9]
Andrews (Ref 63)	$539 - (423C + 30.4Mn + 12.1Cr + 17.7Ni + 7.5Mo)$	212.2	[12.2, 62.2]
Gooch (Ref 64)	$540 - (497C + 6.3Mn + 10.8Cr + 36Ni + 46.6Mo)$	201.8	[1.8, 51.8]
Self et al. (Ref 65)	$526 - (354C + 29.7Mn + 31.7Si + 12.5Cr + 17.4Ni + 20.8Mo)$	199.4	[-0.6, 49.4]
Higgins (Ref 20)	$500 - (333C + 34Mn + 35V + 20Cr + 17Ni + 11Mo + 10Cu + 5W + 15Co - 30Al)$	97.0	[-103, -53]

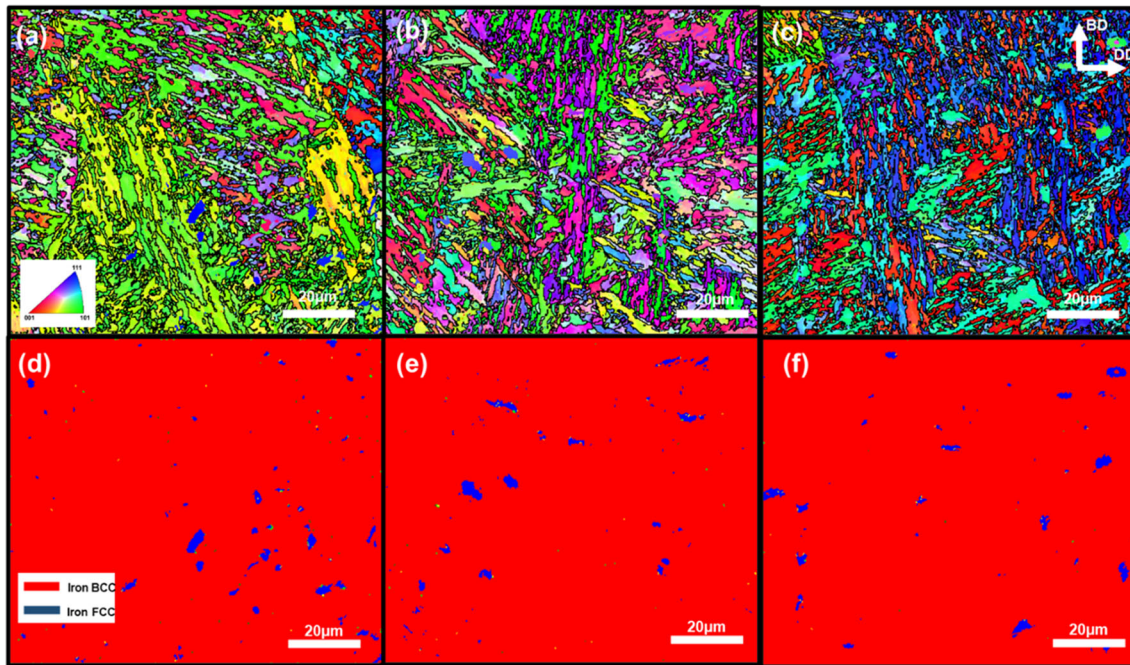


Fig. 5 Inverse pole figure and grain boundary maps for the (a) bottom, (b) middle and (c) top regions of the deposited wall, EBSD phase distribution map of the (d) bottom, (e) middle and (f) top regions, and grain size distribution of the (g) bottom, (h) middle and (i) top regions

of the retained austenite phase with face-centered cubic (FCC) structure is distinguished in the phase maps of all regions (~11%). Retained austenite phase is observed to distribute randomly in the structure, and no significant change in the volume fraction of the austenite phase was detected from the bottom to the top layers.

The resulting pole figures of the formed BCC phase (the tempered martensite laths combined with the delta ferrite phase) and FCC phase (the retained austenite) in the structures of the bottom, middle and top samples for planes of $\{100\}$, $\{110\}$ and $\{111\}$ are shown in Fig. 6. A strong cubic texture with few pole components is observed for $\{100\}$ and $\{111\}$ family of planes of the BCC structure for the bottom, middle and top layers. The detected strong alignment of the $\{100\}$ poles implies the formation of a strong texture during the solidification process (Ref 43–45) and the subsequent multi-step heat treatment cycles associated with the deposition process. There are also misalignments between the detected $\{100\} \langle 100 \rangle$ texture and the building direction of all three samples, ascribed to the fact that the epitaxial growth direction of the grains (aligned with the $\langle 001 \rangle$ direction) is expected to be perpendicular to the melt pool boundaries, which are not necessarily perpendicular to the building direction. A similar misalignment between the grain growth direction and the building direction of AM-fabricated parts have been reported in previous studies (Ref 46–49). A single high-intensity pole is observed for the $\{110\}$, the most close-packed plane in the BCC phase, which is relatively aligned with the deposition direction (DD), in all regions of the deposited wall. This can potentially facilitate the plastic deformation along the deposition direction of the fabricated wall, if the microstructure of the sample can accommodate some degree of plastic strain.

A significantly strong texture was detected for the retained austenite (the FCC phase) in $\{100\}$ planes at all regions, representing the strong texture in the primary austenite grains in

each region with some degree of misorientation relative to the building direction, consistent with the $\{100\}$ PF of the BCC phase. Overall, the EBSD analysis of the bottom, middle and the top layers exhibited nearly the same crystallographic orientation, indicating similar distribution of texture for both martensite and retained austenite phases from the bottom to the top regions of the fabricated wall.

3.2 Mechanical Properties

3.2.1 Hardness. Figure 7 depicts the average Vickers hardness values of three different regions of the as-printed wall. Multiple indentations were taken from three layers located within each of the three investigated regions. As shown in Fig. 7, a significant increase in hardness was detected for the top region. The hardness value of 732 ± 36.3 HV was measured for the top region, as compared to 620 ± 36.3 HV and 637 ± 42.7 HV for the bottom and middle regions, respectively. A similar trend in the hardness values of the WAAM-fabricated 13Cr SS part along the building direction was reported in an earlier study (Ref 36). A higher hardness value for the last deposited layer was also noted for a WAAM-fabricated Inconel 625 (Ref 50). The higher hardness values in the final layers can result from the fact that these layers have undergone a smaller number of in situ re-heating cycles than their underlying layers. Low tempering temperatures of 300°C have been reported not to affect the hardness of the 13Cr stainless steel material when tempering for 2.5 h, while higher tempering temperatures of 550°C and 700°C lowered the hardness (Ref 51). As already stated, the temperature of a specific underlying layer is periodically re-heated as new layers are deposited on its top. At a certain point, the temperature of this layer no longer reaches the sufficient temperature required for the stress relieving and subsequent tempering of the martensitic matrix, and consequently, the hardness stabilizes,

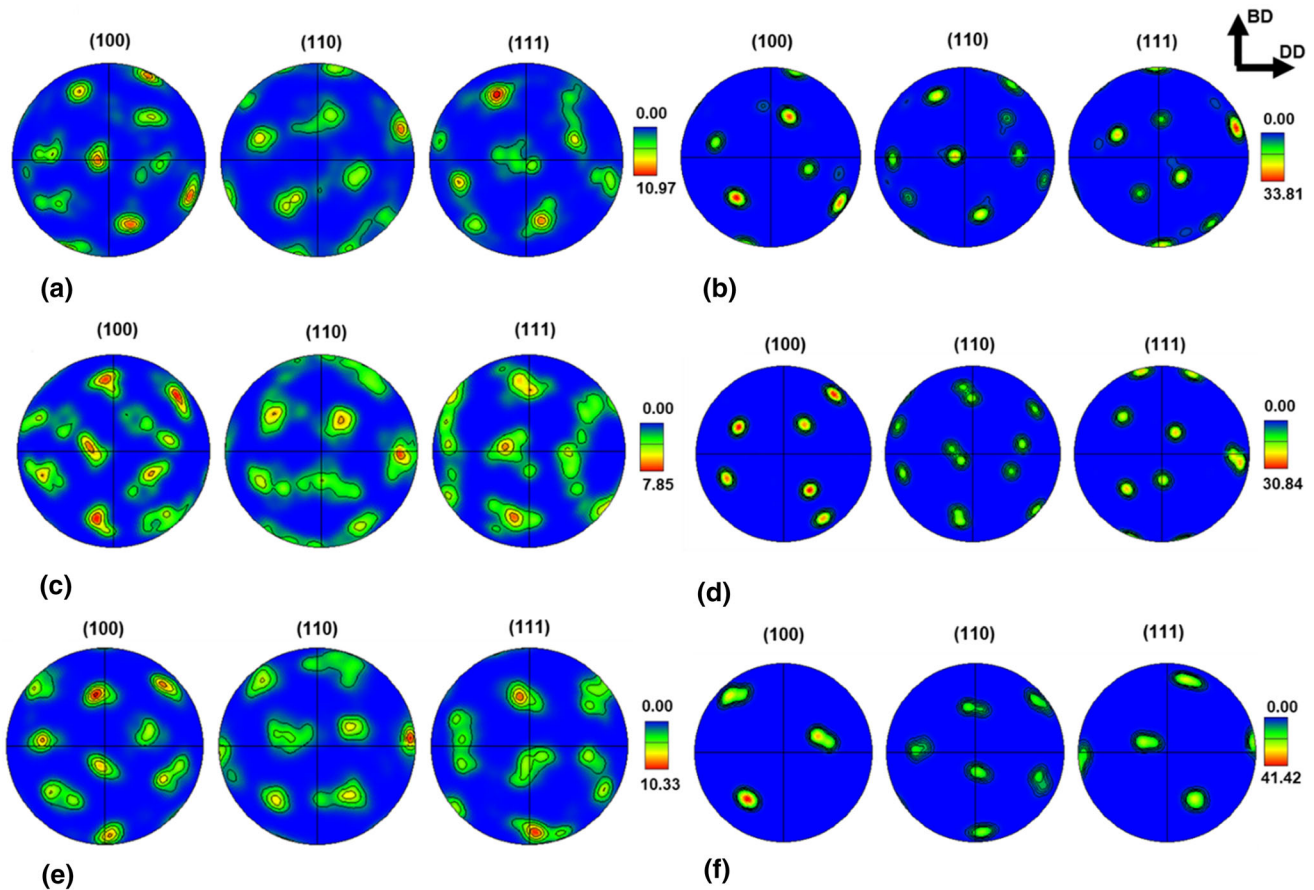


Fig. 6 PF of the martensite phase formed in the (a) bottom, (c) middle and (e) top regions, PF of the austenite phase formed in the (b) bottom, (d) middle and (f) top regions

approximately around 450 °C (Ref 52). However, for the top layers the number of in situ re-heating cycles is lower than the middle or the bottom layers, resulting in the formation of harder top layers in as-printed condition (Ref 40).

A higher volume fraction of retained austenite has been also reported to lower the hardness in SS family (Ref 27, 53). However, due to the lack of sufficient localized re-heating treatment in the top layers and the homogeneous distribution of retained austenite from the bottom to the top layers, the formation of retained austenite in the WAAM-fabricated AISI 420 SS wall in this study did not seem to be the dictating factor in controlling the as-printed hardness of the alloy.

3.2.2 Tensile Properties. Figure 8 shows the stress–strain graphs obtained from uniaxial tensile testing of the samples taken from the horizontal direction (deposition direction) in the bottom, middle and top regions along with the building direction denoted as vertical. As can be observed from the graphs, the mechanical properties of the fabricated part under uniaxial tensile loading seem to be very consistent at the bottom and middle regions along both horizontal and vertical directions with comparable values of fracture strength and elongation, suggesting an isotropic response in the mechanical properties. However, the horizontal sample from the top region (horizontal top) differs from the other three by demonstrating lower properties, fracturing at both lower strength and elongation. The extracted values of the ultimate tensile strength (UTS), elongation and yield strength (YS) of all tested samples are

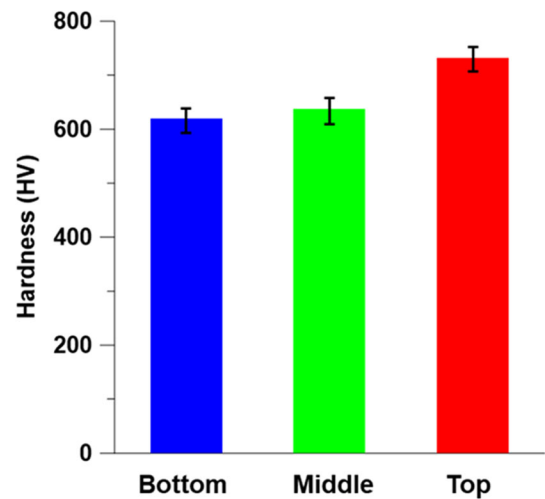


Fig. 7 Vickers microhardness results of the bottom, middle and top regions of the as-printed wall

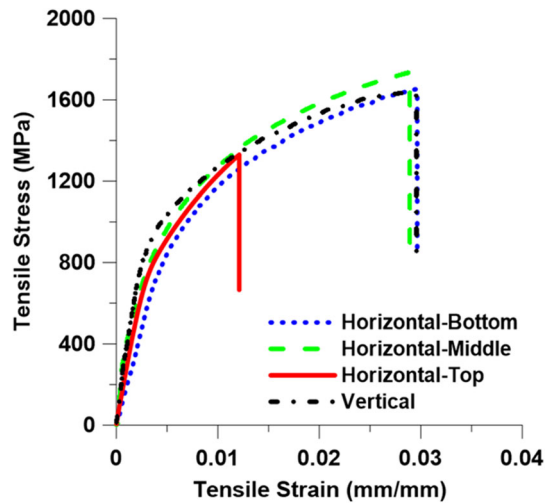


Fig. 8 Stress–strain graphs of the horizontal samples machined from the bottom, middle and the top regions of the fabricated wall and the vertical tensile specimens

Table 4 Tensile test values for the horizontal samples from the bottom, middle and the top regions, and the vertical samples

Sample	YS, MPa	UTS, MPa	Elongation, %
Horizontal bottom	987 ± 26.2	1654 ± 43.8	2.97 ± 0.24
Horizontal middle	933 ± 24.7	1733 ± 45.9	2.89 ± 0.24
Horizontal top	907 ± 24.0	1330 ± 35.2	1.21 ± 0.10
Vertical	1027 ± 27.2	1633 ± 43.3	2.96 ± 0.24

summarized in Table 4. None of the samples experienced necking before fracture, indicating that all samples fractured when reached to their UTS points. Consistent with the observed more brittle response of the horizontal top sample herein, Ge et al. (Ref 10) reported a more brittle fracture for the top layer of a CMT WAAM-2Cr13 thin-wall part than the underlying layers as a result of the formed fully martensitic microstructure in the top layer.

It is also worth noting that retained austenite can transform into martensite during uniaxial loading, leading to an increase in strength and ductility for stainless steel alloys, known as transformation-induced plasticity (TRIP) (Ref 54). Random crystallographic texture has been reported to promote TRIP during uniaxial tension for austenitic steels (Ref 55). Even though the samples in the present study show high strength, the fracture mode of the samples is predominantly brittle, indicating little to no improved plasticity induced by the transformation of retained austenite to martensite. The similarity of the obtained EBSD results for all regions implies that solidification-induced texture in the fabricated samples is not the driving force for the top region’s distinct mechanical properties.

Delta ferrite has been also reported to have a positive impact on elongation, while deteriorating the overall strength of martensitic stainless steels (Ref 56). A high amount of retained delta ferrite in the microstructure has been shown to accelerate the cracking of AISI 420 SS weld (Ref 57). Therefore, the harder nature of less tempered martensite in the top layers

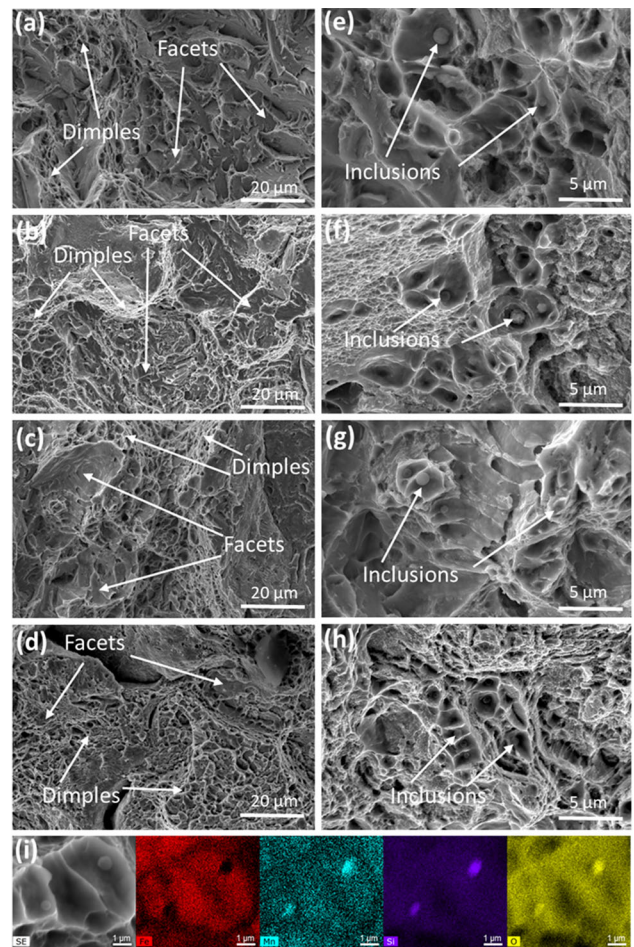


Fig. 9 SEM images of the fractured surfaces of the tensile samples showing a mixed-mode fracture along with the presence of inclusions at the center of the dimples. (a, e), (b, f), (c, g) and (d, h) correspond to the horizontal bottom, middle, top and vertical samples, respectively. (i) shows the SEM image and elemental distribution maps taken from the inclusions

accompanied with their higher content of delta ferrite has resulted in the lower strength and more brittle fracture of the top region under uniaxial tensile loading compared with the other regions.

3.2.3 Fractography. Figure 9 shows the SEM images depicting the fractured surfaces of the vertical and horizontal tensile samples from the bottom, middle and top regions. Cleavage facets and dimples indicated by the arrows in the lower magnification images can be seen on all fractured surfaces, indicating that a mixed-mode brittle and ductile fractures has occurred. Higher-magnification images of the dimpled areas also revealed the presence of inclusion particles at the center of the dimples. These inclusions lacked in Fe and consisted mainly of Mn, Si and O, suggesting their MnO-SiO₂ nature. Furthermore, the dimples formed on the fractured surface of the top layer were found to be shallower than those on the other samples, consistent with the measured lower plastic strain for the horizontal top sample. Similar mixed-mode fractures at a relatively low elongation of 2% have been reported for 13Cr SS alloy tempered at 300 °C (Ref 51). Previous studies have also shown similar variations of fracture

modes from ductile to mixed and brittle modes from the bottom to the middle and top regions, respectively, of a CMT WAAM-fabricated 2Cr13 part (Ref 10). Inclusions, on the other hand, can lead to the formation of voids, which can affect the fracture process of a material (Ref 58). Similar inclusion particles were found on the fractured surfaces of tensile specimens for a Cr-Ni SS produced by both single- and double-wire feed plasma arc AM (Ref 59). An increasing amount of inclusions can facilitate voids nucleation, which can lead to a decreasing active load area for the specimen under tension, ultimately resulting in a premature fracture (Ref 58). Contrarily, a high number of nucleation sites for microvoids can delay the fracture, thus increasing the ductility of the material (Ref 60).

4. Conclusions

The present study investigated the microstructure and mechanical properties of an AISI 420 multilayer single-bead part fabricated using WAAM technology. The following conclusions can be made:

1. The as-printed wall revealed a multi-phase microstructure consisting of a martensitic matrix along with secondary retained austenite and delta ferrite phases. The stability of delta ferrite at room temperature was correlated with high cooling rates during solidification combined with the high content of ferrite stabilizing elements, such as chromium, in the alloy.
2. The morphology of delta ferrite phase in the top region varied from the other regions and was characterized by having a vermicular-shaped morphology formed along the primary austenite grain boundaries as compared to the less continuous network of delta ferrite formed in lower regions. This was due to the heat from newly deposited layers, retransforming a portion of the delta ferrite to austenite during heating and ultimately transforming to martensite upon cooling.
3. The lower M_f temperature of the alloy than the room temperature led to the stability of retained austenite in the microstructure at room temperature.
4. Significantly higher hardness values were found for the top layers compared with the bottom and middle layers, which both exhibited similar hardness values. The increase in hardness at top layers was observed due to the lack of sufficient in situ re-heating treatment from above-deposited layers.
5. The high hardness values of the deposited wall resulted in high strength and low elongation fractures under uniaxial tensile loading. The top region along the deposition direction fractured at lower elongation and strength than the horizontal bottom, middle and vertical samples, which all revealed a similar mechanical response under uniaxial tension. The measured texture of the fabricated sample at different regions was found to be relatively the same, suggesting that the detected higher amount of delta ferrite phase along with the harder nature of the formed martensite in the top region was the determining factors in controlling the lower tensile properties of the top layer.
6. All tensile specimens experienced a mixed-mode fracture with inclusion particles present inside the formed dim-

ples. These particles contributed to the brittle nature of the fracture by decreasing the active load area of the specimen under tension.

Acknowledgements

The authors would like to thank the support of Suncor Energy, Natural Sciences and Engineering Research Council of Canada (NSERC) [grant number RGPIN-2017-04368], Dalhousie University and the Memorial University of Newfoundland, for sponsoring this work.

References

1. Y. Kok, X.P. Tan, P. Wang et al., Anisotropy and Heterogeneity of Microstructure and Mechanical Properties in Metal Additive Manufacturing: A Critical Review, *Mater. Des.*, 2018 <https://doi.org/10.1016/j.matdes.2017.11.021>
2. T. Duda, L.V. Raghavan, 3D Metal Printing Technology. IFAC-PapersOnLine. (2016) <https://doi.org/10.1016/j.ifacol.2016.11.111>
3. T.D. Ngo, A. Kashani, G. Imbalzano et al., Additive Manufacturing (3D printing): A Review of Materials, Methods, Applications and Challenges. *Compos. Part B Eng.* (2018)
4. L. Wang, J. Xue and Q. Wang, Correlation Between Arc Mode, Microstructure, and Mechanical Properties During Wire Arc Additive Manufacturing of 316L Stainless Steel, *Mater. Sci. Eng. A*, 2019 <https://doi.org/10.1016/j.msea.2019.02.078>
5. J.G. Lopes, C.M. Machado, V.R. Duarte et al., Effect of Milling Parameters on HSLA Steel Parts Produced by Wire and Arc Additive Manufacturing (WAAM), *J. Manuf. Process.*, 2020, **59**, p 739–749. <https://doi.org/10.1016/j.jmapro.2020.10.007>
6. T.A. Rodrigues, V.R. Duarte, D. Tomás et al., In-situ Strengthening of a High Strength Low Alloy Steel During Wire and Arc Additive Manufacturing (WAAM), *Addit. Manuf.*, 2020, **34**, 101200. <https://doi.org/10.1016/j.addma.2020.101200>
7. Z. Zeng, B.Q. Cong, J.P. Oliveira et al., Wire and Arc Additive Manufacturing of a Ni-rich NiTi Shape Memory Alloy: Microstructure and Mechanical Properties, *Addit. Manuf.*, 2020, **32**, 101051. <https://doi.org/10.1016/j.addma.2020.101051>
8. J. Ge, T. Ma, Y. Chen et al., Wire-Arc Additive Manufacturing H13 Part: 3D Pore Distribution, Microstructural Evolution, and Mechanical Performances, *J. Alloys Compd.*, 2019 <https://doi.org/10.1016/j.jallcom.2018.12.274>
9. A. Vahedi Nemani, M. Ghaffari and A. Nasiri, On the Post-Printing Heat Treatment of a Wire Arc Additively Manufactured ER70S Part, *Materials (Basel)*, 2020 <https://doi.org/10.3390/ma13122795>
10. J. Ge, J. Lin, Y. Chen et al., Characterization of Wire Arc Additive Manufacturing 2Cr13 Part: Process Stability, Microstructural Evolution, and Tensile Properties, *J. Alloys Compd.*, 2018 <https://doi.org/10.1016/j.jallcom.2018.03.222>
11. M. Rafieazad, M. Ghaffari, A. Vahedi Nemani and A. Nasiri, Microstructural Evolution and Mechanical Properties of a Low-Carbon Low-Alloy Steel Produced by Wire Arc Additive Manufacturing, *Int. J. Adv. Manuf. Technol.*, 2019 <https://doi.org/10.1007/s00170-019-04393-8>
12. T.A. Rodrigues, V. Duarte, J.A. Avila et al., Wire and Arc Additive Manufacturing of HSLA Steel: Effect of Thermal Cycles on Microstructure and Mechanical Properties, *Addit. Manuf.*, 2019, **27**, p 440–450. <https://doi.org/10.1016/j.addma.2019.03.029>
13. X. Xu, S. Ganguly, J. Ding et al., Microstructural Evolution and Mechanical Properties of Maraging Steel Produced by Wire + Arc Additive Manufacturing Process, *Mater. Charact.*, 2018 <https://doi.org/10.1016/j.matchar.2017.12.002>
14. M. Ghaffari, A. Vahedi Nemani, M. Rafieazad and A. Nasiri, Effect of Solidification Defects and HAZ Softening on the Anisotropic Mechanical Properties of a Wire Arc Additive-Manufactured Low-Carbon Low-Alloy Steel Part, *JOM*, 2019 <https://doi.org/10.1007/s11837-019-03773-5>

15. J.J. Lewandowski and M. Seifi, Metal Additive Manufacturing: A Review of Mechanical Properties, *Ann. Rev. Mater. Res.*, 2016 <https://doi.org/10.1146/annurev-matsci-070115-032024>
16. T.A. Rodrigues, V. Duarte, R.M. Miranda et al., Current Status and Perspectives on Wire and Arc Additive Manufacturing (WAAM), *Materials (Basel)*, 2019 <https://doi.org/10.3390/ma12071121>
17. F. Hejripour, F. Binesh, M. Hebel and D.K. Aidun, Thermal Modeling and Characterization of Wire Arc Additive Manufactured Duplex Stainless Steel, *J. Mater. Process. Technol.*, 2019 <https://doi.org/10.1016/j.jmatprotec.2019.05.003>
18. M.L. Griffith, M.T. Ensz, J.D. Puskar et al., Understanding the Microstructure and Properties of Components Fabricated by Laser Engineered Net Shaping (LENS), *Mater. Res. Soc. Symp. Proc.*, 2000 <https://doi.org/10.1557/PROC-625-9>
19. C.X. Li and T. Bell, Corrosion Properties of Plasma Nitrided AISI 410 Martensitic Stainless Steel in 3.5% NaCl and 1% HCl Aqueous Solutions, *Corros. Sci.*, 2006 <https://doi.org/10.1016/j.corsci.2005.08.011>
20. R.A. Higgins, Engineering Metallurgy Part I Applied Physical Metallurgy, 6th ed., (1993)
21. M. Kazempour, S. Salahi and A. Nasiri, Box-Behnken Design Approach Toward Predicting the Corrosion Response of 13Cr Stainless Steel, *Corrosion*, 2020 <https://doi.org/10.5006/3429>
22. L.D. Barlow and M. Du Toit, Effect of Austenitizing Heat Treatment on the Microstructure and Hardness of Martensitic Stainless Steel AISI 420, *J. Mater. Eng. Perform.*, 2012 <https://doi.org/10.1007/s11665-011-0043-9>
23. S. Salahi, M. Kazempour, A. Nasiri, Effect of Uniaxial Tension-Induced Plastic Strain on the Microstructure and Corrosion Behavior of 13Cr Martensitic Stainless Steel. *Corrosion* (2020)
24. S. Salahi, M. Kazempour and A. Nasiri, Effects of Microstructural Evolution on the Corrosion Properties of AISI 420 Martensitic Stainless Steel During Cold Rolling Process, *Mater. Chem. Phys.*, 2021 <https://doi.org/10.1016/j.matchemphys.2020.123916>
25. C.O.A. Olsson and D. Landolt, Passive Films on Stainless Steels - Chemistry, Structure and Growth, *Electrochim. Acta*, 2003 [https://doi.org/10.1016/S0013-4686\(02\)00841-1](https://doi.org/10.1016/S0013-4686(02)00841-1)
26. H. Zhang, Y.L. Zhao and Z.D. Jiang, Effects of Temperature on the Corrosion Behavior of 13Cr Martensitic Stainless Steel During Exposure to CO₂ and Cl⁻ Environment, *Mater. Lett.*, 2005 <https://doi.org/10.1016/j.matlet.2005.06.002>
27. P.D. Bilmes, M. Solari and C.L. Llorente, Characteristics and Effects of Austenite Resulting from Tempering of 13Cr-NiMo Martensitic Steel Weld Metals, *Mater. Charact.*, 2001 [https://doi.org/10.1016/S1044-5803\(00\)00099-1](https://doi.org/10.1016/S1044-5803(00)00099-1)
28. J. Lunde, M. Kazempour, S. Salahi, A. Nasiri, Microstructure and Mechanical Properties of AISI 420 Stainless Steel Produced by Wire Arc Additive Manufacturing. *Min. Metals Mater. Series* (2020)
29. M. Kazempour, J.H. Lunde, S. Salahi, A. Nasiri, On the Microstructure and Corrosion Behavior of Wire Arc Additively Manufactured AISI 420 Stainless Steel. *Min. Metals Mater. Series* (2020)
30. S.H. Baghjari and S.A.A. Akbari Mousavi, Effects of Pulsed Nd: YAG Laser Welding Parameters and Subsequent Post-Weld Heat Treatment on Microstructure and Hardness of AISI 420 Stainless Steel, *Mater. Des.*, 2013 <https://doi.org/10.1016/j.matdes.2012.06.027>
31. S.Y. Tarasov, A.V. Filippov, N.N. Shamarin et al., Microstructural Evolution and Chemical Corrosion of Electron Beam Wire-Feed Additively Manufactured AISI 304 Stainless Steel, *J. Alloys Compd.*, 2019 <https://doi.org/10.1016/j.jallcom.2019.06.246>
32. J. Ge, J. Lin, H. Fu et al., Tailoring Microstructural Features of Wire Arc Additive Manufacturing 2Cr13 Part Via Varying Inter-Layer Dwelling Time, *Mater. Lett.*, 2018 <https://doi.org/10.1016/j.matlet.2018.08.037>
33. J.C. Lippold and D.J. Kotecki, *Welding Metallurgy of Stainless Steels – Lippold.Pdf*, Wiley, Hoboken, New Jersey, 2005
34. M. Bahrami Balajaddeh and H. Naffakh-Moosavy, Pulsed Nd:YAG Laser Welding of 17–4 PH Stainless Steel: Microstructure, Mechanical Properties, and Weldability Investigation, *Opt. Laser Technol.*, 2019 <https://doi.org/10.1016/j.optlastec.2019.105651>
35. J. Ge, J. Lin, H. Fu et al., A Spatial Periodicity of Microstructural Evolution and Anti-Indentation Properties of Wire-Arc Additive Manufacturing 2Cr13 Thin-Wall Part, *Mater. Des.*, 2018 <https://doi.org/10.1016/j.matdes.2018.09.021>
36. J. Ge, J. Lin, Y. Lei and H. Fu, Location-Related Thermal History, Microstructure, and Mechanical Properties of Arc Additively Manufactured 2Cr13 Steel Using Cold Metal Transfer Welding, *Mater. Sci. Eng. A*, 2018 <https://doi.org/10.1016/j.msea.2017.12.076>
37. F.B. Pickering, The Metallurgical Evolution of Stainless Steels, a Discriminative Selection of Outstanding Articles and Papers from the Scientific Literature. *Am. Soc. Met.* (1979)
38. P. Krakhmalev, I. Yadroitsava, G. Fredriksson and I. Yadroitsev, In Situ Heat Treatment in Selective Laser Melted Martensitic AISI 420 Stainless Steels, *Mater. Des.*, 2015 <https://doi.org/10.1016/j.matdes.2015.08.045>
39. A. Caballero, J. Ding, S. Ganguly and S. Williams, Wire + Arc Additive Manufacture of 17–4 PH Stainless Steel: Effect of Different Processing Conditions on Microstructure, Hardness, and Tensile Strength, *J. Mater. Process. Technol.*, 2019 <https://doi.org/10.1016/j.jmatprotec.2019.01.007>
40. Y. Ali, P. Henckell, J. Hildebrand et al., Wire Arc Additive Manufacturing of Hot Work Tool Steel with CMT Process, *J. Mater. Process. Technol.*, 2019 <https://doi.org/10.1016/j.jmatprotec.2019.01.034>
41. A. Vahedi Nemani, M. Ghaffari, S. Salahi et al., Effect of Interpass Temperature on the Formation of Retained Austenite in a Wire Arc Additive Manufactured ER420 Martensitic Stainless Steel, *Mater. Chem. Phys.*, 2021, **266**, 124555. <https://doi.org/10.1016/j.matchemphys.2021.124555>
42. S.Y. Lu, K.F. Yao, Y.B. Chen et al., The Effect of Tempering Temperature on the Microstructure and Electrochemical Properties of a 13 wt.% Cr-Type Martensitic Stainless Steel, *Electrochim. Acta*, 2015 <https://doi.org/10.1016/j.electacta.2015.02.038>
43. S. Li, I.J. Beyerlein and M.A.M. Bourke, Texture Formation During Equal Channel Angular Extrusion of fcc and bcc Materials: Comparison with Simple Shear, *Mater. Sci. Eng. A*, 2005 <https://doi.org/10.1016/j.msea.2004.11.032>
44. D. Raabe and K. Luecke, Rolling and Annealing Textures of bcc Metals, *Mater. Sci. Forum*, 1994
45. S. Suwas and R. Kumar Ray, *Crystallographic Texture of Materials*, Springer, London, 2014
46. P. Fathi, M. Rafieezad, X. Duan et al., On Microstructure and Corrosion Behaviour of AlSi10Mg Alloy with Low Surface Roughness Fabricated by Direct Metal Laser Sintering, *Corros. Sci.*, 2019 <https://doi.org/10.1016/j.corsci.2019.05.032>
47. M. Ghaffari, A. Vahedi Nemani and A. Nasiri, Interfacial Bonding Between a Wire Arc Additive Manufactured 420 Martensitic Stainless Steel Part and its Wrought Base Plate, *Mater. Chem. Phys.*, 2020 <https://doi.org/10.1016/j.matchemphys.2020.123199>
48. A. Vahedi Nemani, M. Ghaffari and A. Nasiri, Comparison of Microstructural Characteristics and Mechanical Properties of Ship-building Steel Plates Fabricated by Conventional Rolling Versus Wire Arc Additive Manufacturing, *Addit. Manuf.*, 2020 <https://doi.org/10.1016/j.addma.2020.101086>
49. A. Shahriari, L. Khaksar, A. Nasiri et al., Microstructure and Corrosion Behavior of a Novel Additively Manufactured Maraging Stainless Steel, *Electrochim. Acta*, 2020 <https://doi.org/10.1016/j.electacta.2020.135925>
50. W. Yangfan, C. Xizhang and S. Chuanchu, Microstructure and Mechanical Properties of Inconel 625 Fabricated by Wire-Arc Additive Manufacturing, *Surf. Coat. Technol.*, 2019 <https://doi.org/10.1016/j.surfcoat.2019.05.079>
51. S.K. Bonagani, B. Vishwanadh, S. Tenneti et al., Influence of Tempering Treatments on Mechanical Properties and Hydrogen Embrittlement of 13 wt% Cr Martensitic Stainless Steel, *Int. J. Press Vessel. Pip.*, 2019, **176**, 103969. <https://doi.org/10.1016/j.ijpvp.2019.103969>
52. ASM International (2016) One Minute Mentor: Tempering Corrosion-Resistant Tool Steels. https://www.asminternational.org/web/hts/news/newswire/-/journal_content/56/10192/26295783/NEWS. Accessed 4 Sep 2020
53. L. Pan, C.T. Kwok and K.H. Lo, Enhancement in Hardness and Corrosion Resistance of AISI 420 Martensitic Stainless Steel Via Friction Stir Processing, *Surf. Coat. Technol.*, 2019 <https://doi.org/10.1016/j.surfcoat.2018.10.023>
54. J. Shi, X. Sun, M. Wang et al., Enhanced Work-Hardening Behavior and Mechanical Properties in Ultrafine-Grained Steels with Large-

- Fractioned Metastable Austenite, *Scr. Mater.*, 2010 <https://doi.org/10.1016/j.scriptamat.2010.06.023>
55. E. Polatidis, W.N. Hsu, M. Šmíd et al., Suppressed Martensitic Transformation Under Biaxial Loading in Low Stacking Fault Energy Metastable Austenitic Steels, *Scr. Mater.*, 2018 <https://doi.org/10.1016/j.scriptamat.2017.12.026>
 56. L. Schäfer, Influence of Delta Ferrite and Dendritic Carbides on the Impact and Tensile Properties of a Martensitic Chromium Steel, *J. Nucl. Mater.*, 1998 [https://doi.org/10.1016/S0022-3115\(98\)00200-1](https://doi.org/10.1016/S0022-3115(98)00200-1)
 57. Y.C. Lin, S.C. Chen, Effect of Residual Stress on Thermal Fatigue in a Type 420 Martensitic Stainless Steel Weldment. *J. Mater. Process. Technol.* (2003)
 58. X. Zhang, Q. Zhou, K. Wang et al., Study on Microstructure and Tensile Properties of High Nitrogen Cr-Mn Steel Processed by CMT Wire and Arc Additive Manufacturing, *Mater. Des.*, 2019 <https://doi.org/10.1016/j.matdes.2019.107611>
 59. Y. Feng, B. Zhan, J. He and K. Wang, The Double-Wire Feed and Plasma Arc Additive Manufacturing Process for Deposition in Cr-Ni Stainless Steel, *J. Mater. Process. Technol.*, 2018 <https://doi.org/10.1016/j.jmatprotec.2018.04.040>
 60. M.K. Alam, M. Mehdi, R.J. Urbanic, A. Edrissy, Mechanical Behavior of Additive Manufactured AISI 420 Martensitic Stainless Steel. *Mater. Sci. Eng. A* (2020)
 61. K.J. Irvine, D.J. Crowe and F.B. Pickering, The Physical Metallurgy of 12% Chromium Steels, *J. Iron Steel Inst.*, 1960, **195**, p 386–405
 62. W. Steven and A.G. Haynes, The Temperature of Formation of Martensite and Bainite in Low-Alloy Steels, *J. Iron Steel Inst.*, 1956, **183**, p 349–359
 63. K. Andrews, Empirical Formulae for the Calculation of Some Transformation Temperatures, *J. Iron Steel Inst.*, 1965, **203**, p 721–727
 64. G.T. Gooch, Welding Martensitic Stainless Steels, *Weld Inst. Res. Bull.*, 1977, **18**, p 343–349
 65. J.A. Self, D.L. Olson, R. Eg, The stability of austenitic weld metal. *Proc IMCC* (1984)

Publisher's Note Springer Nature remains neutral with regard to jurisdictional claims in published maps and institutional affiliations.